Grégory Bièvre · Denis Jongmans · David Goutaland · Erwan Pathier · Vilma Zumbo

Geophysical characterization of the lithological control on the kinematic pattern in a large clayey landslide (Avignonet, French Alps)

Abstract Lithology variation is known to have a major control on landslide kinematics, but this effect may remain unnoticed due to low spatial coverage during investigation. The large clayey Avignonet landslide (French Alps) has been widely studied for more than 35 years. Displacement measurements at 38 geodetic stations over the landslide showed that the slide surface velocity dramatically increases below an elevation of about 700 m and that the more active zones are located at the bottom and the south of the landslide. Most of the geotechnical investigation was carried out in the southern part of the landslide where housing development occurred on lacustrine clay layers. In this study, new electrical prospecting all across the unstable area revealed the unexpected presence of a thick resistive layer covering the more elevated area and overlying the laminated clays, which is interpreted as the lower part of moraine deposits. The downslope lithological boundary of this layer was found at around 700 m asl. This boundary coincides with the observed changes in slide velocity and in surface roughness values computed from a LiDAR DTM acquired in 2006. This thick permeable upper layer constitutes a water reservoir, which is likely to influence the hydromechanical mechanism of the landslide. The study suggests a major control of vertical lithological variations on the landslide kinematics, which is highlighted by the relation between slide velocity and electrical resistivity.

Keywords Clayey landslide · Slide velocity · Deformation pattern · Hydrogeology · Geophysics · Lithological control

Introduction

Slow-moving landslides frequently affect gentle slopes made of clayey formations, with volumes which can range from a few cubic metres to several tens of millions of cubic metres (e.g. Kelsey 1978; Iverson and Major 1987; Zhang et al. 1991; Bovis and Jones 1992; Picarelli 2000; Eilertsen et al. 2008; Mackey et al. 2009). These landslides frequently exhibit sudden acceleration phases and flows, which can be triggered by changes in the stress field (pore pressure increase, loading, and erosion) or modifications in the soil characteristics (weathering, leaching or pollutant infiltration; Picarelli et al. 2004; Van Asch et al. 2006; Eilertsen et al. 2008). Understanding landslide behaviour first requires the characterization of the ground surface kinematics (Delacourt et al. 2007), which can be achieved through accurate but punctual measurements, like GPS or optical devices (Malet et al. 2002; Stiros et al. 2004; Corsini et al. 2005; Wang 2011), or more recently through dense displacement maps provided by digital photogrammetry (Schwab et al. 2008; Baldi et al. 2008; Mackey et al. 2009; Travelletti et al. 2012), laser scanning (Corsini et al. 2007; Teza et al. 2008; Jaboyedoff et al. 2012; Daehne and Corsini 2013) or Synthetic Aperture Radar Interferometry (InSAR; Rott et al. 1999; Squarzoni et al. 2003; Strozzi et al. 2005; Roering et al. 2009).

Continuous geodetic measurements provide excellent temporal resolution with low spatial resolution. On the contrary, InSAR and laser scanning, whose sensors can be attached to aerial or ground platforms, are limited in terms of temporal resolution. Displacement measurements on clayey landslides usually display a spatially heterogeneous field, with zones of higher activity which can evolve with time (Squarzoni et al. 2003; Corsini et al. 2005; François et al. 2007; Baldi et al. 2008; Travelletti et al. 2013).

Kinematics in clayey landslides has been extensively studied and is classically interpreted as controlled by external factors such as meteorological and/or climatic parameters (rainfall, temperature, snowmelt, etc.; Iverson and Major 1987; Flageollet et al. 1999; Van Asch et al. 1999; Iverson 2000; Aleotti 2004) with a predominant influence of water infiltration inducing mechanical deformations and possible landslide motion (e.g. Iverson 2004; Picarelli et al. 2004; van Asch et al. 2007, 2009; Handwerger et al. 2013). Landsliding and the consecutive deformation (ductile and brittle) might, in turn, modify the ground hydraulic properties (porosity and permeability). This hydromechanical coupling is one of the major slide mechanisms proposed for fine-grained landslides, although other external controlling factors like earthquakes (Keefer 1984, 2002; Rodriguez et al. 1999) and morphology changes resulting from natural erosion or human activities (Eilertsen et al. 2008; Oppikofer et al. 2008) might also play a role.

The slide velocity pattern was also found to vary in space, mostly in relation with the internal factors of the landslide, including weathering, bedrock topography and slip-surface geometry, tectonics and geological heterogeneity (Petley et al. 2005; Corsini et al. 2005; Coe et al. 2009; Bièvre et al. 2011; Travelletti et al. 2013; Guerriero et al. 2014). At the Tessina landslide in northern Italy, which affects quickly evolving Tertiary Flysch deposits, Petley et al. (2005) performed a detailed study of surface displacement series. They distinguished four distinct movement patterns, from slow movements at the crown (about 1 mm/day) to episodic and rapid movements (1 m/day) in the accumulation zone in which mudflows can occur. The pattern evolution is associated with the disintegration and weathering of blocks to fine-grained material during downward movement. Even if this model could fit numerous observations on landslides in clayey soft rocks, additional complexity in the surface and underground kinematic pattern can arise from the other internal factors. In two large clayey landslides, Coe et al. (2009) and Bièvre et al. (2011) showed that the geometry of the underlying bedrock controls the landslide features (ponds and flows) and the deformation pattern (direction and rate) at the surface. Similarly, Guerriero et al. (2014) found evidence of a long-term linkage between the geometry of basal-slip surfaces and surface features and kinematics at the Montaguto earth flow (Southern Italy). Studying the crown of the la Valette landslide (France) in black marls, Travelletti et al. (2013) identified a strong lateral influence of tectonic discontinuities on

the kinematic pattern and on the retrogression mechanism. Finally, the influence of geological heterogeneity on the landslide kinematics was reported at the Corvara landslide (Dolomites, NE Italy) affecting Triassic weak clayey rock masses, whose 3D structure was thoroughly investigated and which was monitored during 1 year using differential GPS and borehole measurements (Corsini et al. 2005). The highest horizontal sliding velocities were recorded not only in the track zone but also in the uppermost part of the accumulation zone. Several slip surfaces were found by borehole devices at depths ranging from 10 to 48 m, and their overlapping and differential activity could explain local increase in sliding velocities. Moreover, some of them were related to coarser horizons which could act as confined aquifers. This vertical geological heterogeneity was thought to have played a significant role in the landslide mechanism and evolution. Although the role of lithology on landslide kinematics has been regularly pointed out at the watershed scale (see above references), to our knowledge, it has rarely been documented over a specific landslide.

The aim of this work is to study such lithological variation and control at the scale of a landslide, using geophysical methods. The study is the large clayey landslide of Avignonet (France), which exhibits a heterogeneous slide velocity field. Although this landslide has been extensively investigated for more than 30 years, this lithological influence has not been reported before, owing to a spatial bias in the geotechnical investigation, which concentrated in inhabited areas. To investigate the whole surface of the landslide (about 1.6×10^6 m²), the electrical resistivity tomography (ERT) technique was applied. The electrical resistivity in clayey landslides is usually low (Jongmans and Garambois 2007; Perrone et al. 2014), and resistivity increase allows detecting the presence of blocks or coarser layers (among others, Lapenna et al. 2005; Jongmans et al. 2009; Lebourg et al. 2010; Chambers et al. 2011). At the Avignonet site, electrical profiles evidenced the presence of a coarser layer, which was validated by hydrogeological observations, permeability measurements and geotechnical tests. Electrical imaging over the whole landslide showed an inverse relation between slide velocity and shallow resistivity values and allowed giving a new interpretation of the velocity field. This case history illustrates the necessity of combining various investigation and monitoring techniques for understanding the mechanism of large landslides.

Study site

Geological context

The Trièves area, located 40 km south of the city of Grenoble (France), is a 300-km² plateau made of Quaternary glaciolacustrine deposits and surrounded by carbonate and crystalline mountain ranges (Fig. 1a). These sediments, which were deposited during the Last Glacial Maximum (LGM) in a glacially dammed lake, show a rhythmic alternation of clayey and silty laminae (millimetre to decimetre thick; Giraud et al. 1991). They overlay a local Quaternary, compact and locally cemented, alluvial formation (made of a succession of sand, gravel and pebble layers) and a Mesozoic bedrock consisting of Jurassic marly limestone (see the geological map and cross section in Fig. 1a, b, respectively). The paleotopography of the former Trièves Lake is irregularly shaped,

inducing a dramatic variation in clay thickness, from 0 to nearly 300 m (Bièvre et al. 2011; Fig. 1b). The laminated clays are locally capped by a few metres to a few tens of metre thick moraine layer (Fig. 1b), evolving into a morainic colluvium of a few metres thick along the slopes. Since the retreat of the glacier 14 ky ago (Brocard et al. 2003), the Drac River has cut into the soft and compact layers and has initiated numerous slides in the clayey formations. Presently, 15 % of the Trièves area is estimated to be sliding (Jongmans et al. 2009).

The main destabilization mechanism in the Trièves area is illustrated along the cross section YY' in Fig. 1c. Water flows downhill in the morainic aquifer until reaching the top of the impermeable laminated clays. Water partially runs off the impervious surface or flows in the thin colluvium layer and infiltrates downslope in the vertical fissures induced by the gravitational movement. This hydrogeological conceptual mechanism has already been proposed on other glacigenic sites (e.g. Gerber and Howard 2000 in Canada) and has already been evidenced as one of the main driving forces of landslide activity in the Trièves area (van Genuchten and van Asch 1988; Vuillermet et al. 1994; van Asch et al. 1996; Bièvre et al. 2012; van der Spek et al. 2013). It contributes to the slope destabilization which, in turn, favours vertical water infiltration.

The Avignonet landslide

The large landslide of Avignonet is located east of the village of Sinard, along the man-made Monteynard Lake (Fig. 1a). This landslide, whose first signs of instability were noticed between 1976 and 1981 (Lorier and Desvarreux 2004), affects a surface of about 1.6×10^6 m². According to the classification proposed by Varnes (1978) and Cruden and Varnes (1996) and its recent update by Hungr et al. (2014), the Avignonet landslide can be defined as a slow clay/silt compound (rototranslational) slide. LiDAR data (airborne light detection and ranging) were collected in November 2006 using a laser scanner mounted on a helicopter (Bièvre et al. 2011). The digital elevation model (DEM) is shown in Fig. 2. The curve-shaped head scarp, which is approximately located at an elevation of 800 m above sea level (asl), corresponds to the eastern border of the Sinard plateau. The landslide is affected by several major internal scarps of a hundred metres long, which can reach 10 m high. The landslide has mainly developed in the clay layer (Fig. 1a). The upper scarp has probably retrogressed, in the same way that the nearby Harmalière landslide behaves (H in Fig 1a; Moulin and Robert 2004), and now affects the morainic cover. Most of the geotechnical investigation in the Avignonet landslide was carried out in the southern most active part during the eighties, where housing development took place in the mid-seventies. Five boreholes (four in 1981 and one in 2009) were drilled in this area (B0 to B4 in Fig. 2) to locate and characterize the rupture surfaces in the clay layer. The first four boreholes were equipped with inclinometers, while the fifth one was cored to allow the lithological and geotechnical characteristics to be studied. Borehole results (Jongmans et al. 2009; Bièvre et al. 2012) detected three main slip surfaces: one at a depth of about 5 m at the bottom of the morainic colluvium layer and two inside the clay layer, between 10 and 20 m and between 40 and 50 m deep, respectively. Three deep boreholes encountered alluvial layers (silts, sands and pebbles) at their bottom, at an elevation between 620 and 636 m asl. Water level is superficial (a few metres below ground surface) with seasonal variations of about 2 to 3 m.
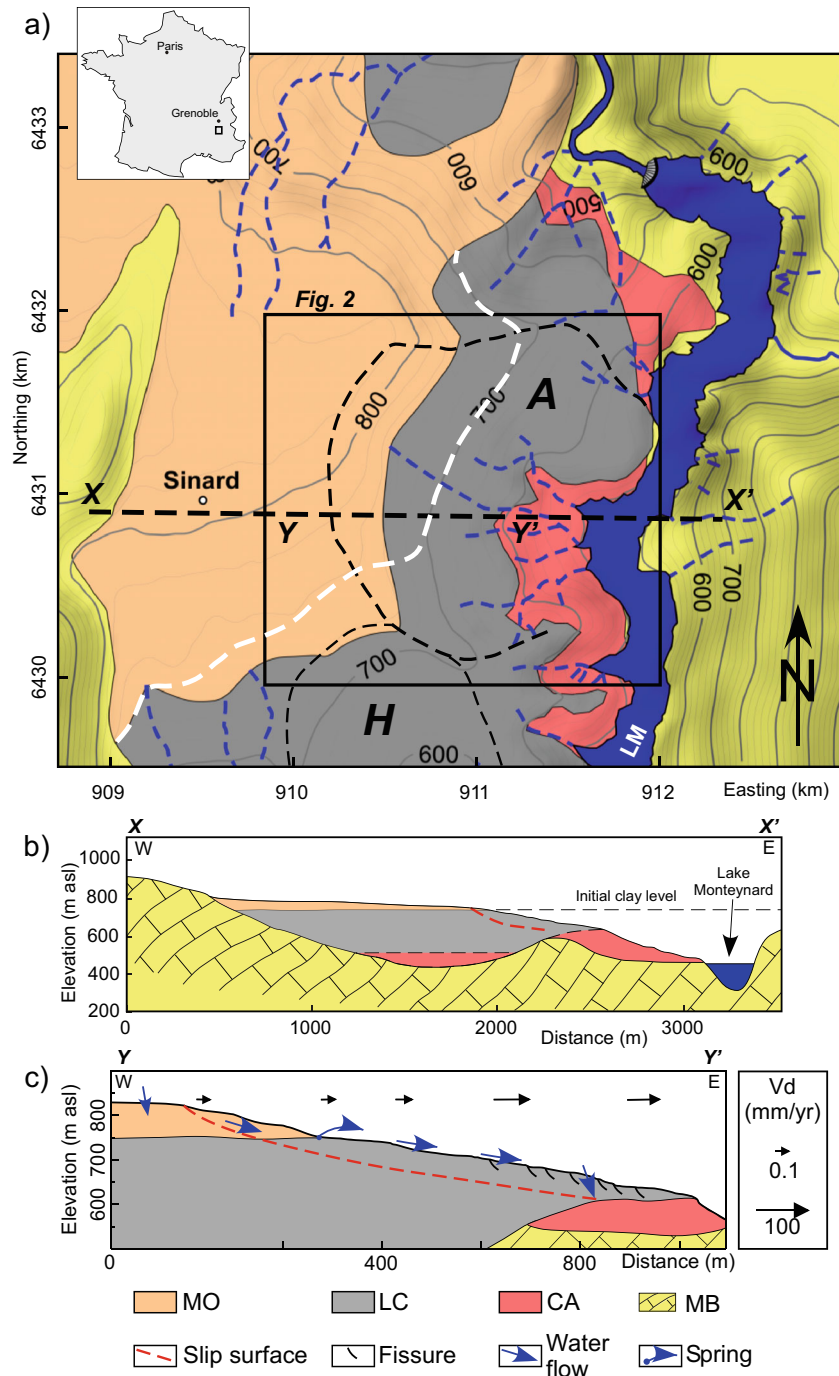
Fig. 1 Location and geology of the study site. **a** Geological map, adapted from Debelmas (1967) and Monjuvent (1973) with the Avignonet (*A*) and Harmalière (*H*) landslide extension and the location of the geological cross sections XX' and YY' shown in **b** and **c**, respectively. The *blue dashed lines* correspond to non-perennial surface flows. The *white dashed line* corresponds to the new interpretation of the base of the moraines. Coordinates are kilometric and expressed in the Lambert-93 French system. **b** Geological cross section XX'. **c** Geological cross section YY'. The morainic colluvium is not represented. *Black and blue arrows* show the slide surface velocities (Vd) and the water flows, respectively. *MB* Mesozoic bedrock, *CA* compact and locally cemented alluvium, *LC* laminated clays, *MO* moraines

Previous geophysical investigations of the landslide (Jongmans et al. 2009; Renalier et al. 2010a, b; Bièvre et al. 2011, 2012) were also focused in the southern part of the Avignonet landslide. Geophysical survey included seismic noise measurements, ERT, P and S-wave seismic refraction tomography and surface wave inversion. ERT and Vp images showed that, below the few metre thick colluvium layer, the underlying material down to 40-m depth is mainly made of saturated clay, with slight variations in Vp (1600 to 1900–2000 m/s) and electrical resistivity (20 to 40 Ω m). On the contrary, Vs exhibits significant lateral and vertical variations (150 to 650 m/s), in agreement with the spatial distribution of slip surfaces and morphological features (Jongmans et al. 2009; Bièvre et al. 2012).
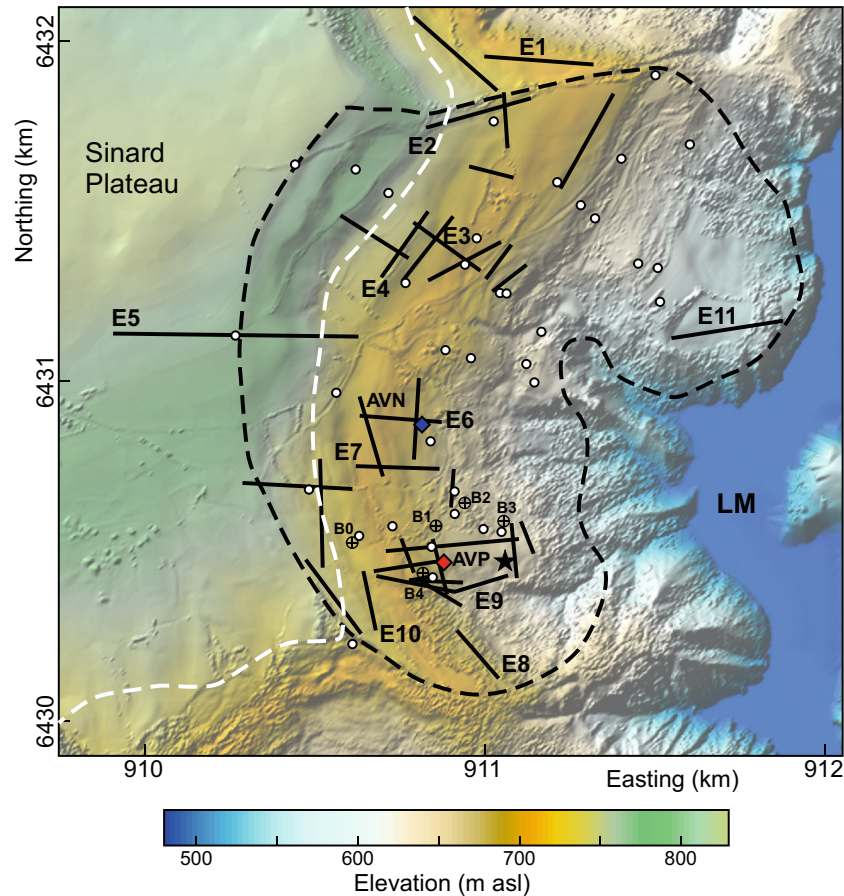
Fig. 2 Morphology of the study area derived from a LiDAR DEM and location of the measurements. *Black dashed line* indicates Avignonet landslide limit; *white dashed line* exhibit the limit between the moraines and the underlying laminated clays according to previous interpretation (Fig. 1); *black line* represents electrical resistivity tomography (ERT) profiles; *E1* to *E11* indicate ERT profile labels detailed in the text; *white dots* indicate geodetic stations; *red and blue dots* show permanent GPS stations AVP and AVN, respectively; *B0* to *B4* represent boreholes; *black star* shows the location from where the picture in Fig. 6 was shot. *LM* Lake Monteynard

Slide velocity pattern

Since 1995, the landslide activity has been monitored twice a year by GPS and tacheometer measurements at 36 geodetic stations (white dots in Fig. 2). Results showed an eastward increase in slide velocity, from less than 1 cm/year in the upper part of the slide to more than 10 cm/year at the toe (Jongmans et al. 2009). The geotechnical and geophysical data acquired so far, predominantly in the southern part of the landslide, provided no insight into the variations observed in the velocity field. This is the main issue addressed in the following sections.

Methods

This study included the performing of an extensive electrical investigation over the landslide, along with a limited number (5) of hydrogeological tests and laboratory identification tests. All slide velocity and morphology data (Jongmans et al. 2009; Kniess et al. 2014) have been gathered and reprocessed.

Surface velocity and morphology

Complementary to the 36 geodetic stations measured twice a year, two permanent GPS stations (labelled AVP and AVN in Fig. 2) were installed in 2007 within the frame of the French Multidisciplinary

Observatory of Versant Instabilities OMIV (http://omiv.osug.fr). Mean annual horizontal velocities and associated standard deviations were calculated at the 38 geodetic stations. These velocities were interpolated to produce a velocity contour map using the geostatistical software Surfer© (Golden Software 2012).

Surface roughness, which represents the degree of elevation variation within an area, has been mapped from a 2-m-resolution LiDAR digital terrain model (DTM; where buildings and vegetation were removed) acquired in 2006 (Kniess 2011; Kniess et al. 2014). A 2-m-spacing grid of roughness values has been computed using the following method. For each point of the roughness grid, a 10-m-radius circle centred on the point is used to crop a local DTM from the main DTM. The main slope direction of the local DTM is estimated and used to determine a 20-m-long upslope-downslope profile centred on the current grid point. This profile direction is more sensitive to detect structures perpendicular to the slide motion, i.e. scarps and fissures. To avoid bias originating from the overall slope, the profile was first detrended. Then, roughness was evaluated using the root mean square deviation (RMSD; Shepard et al. 2001) technique. The 2D grid was achieved by repeating the operation by shifting the current grid point every 2 m (roughness variations are relatively smooth at the grid resolution because local DTMs are overlapping).

Electrical resistivity tomography

Electrical resistivity in a porous medium is a geophysical parameter varying with the porosity, the degree of saturation and the electrical resistivity of the fluid (Archie 1942). In clays, a conductivity term is added to account for the electrical conductivity of the diffuse double layer formed on and between the clayey sheets (Mavko et al. 2009). An external factor influencing the soil resistivity is the temperature, whose effect is, however, limited to a few metres in clayey formations (Travelletti et al. 2011). The ground water level is shallow (a few metres) in the Avignonet landslide, and resistivity values measured at depth greater than 5 m will characterize a saturated soil, with no temperature influence. Any lateral geological facies variations (from clay to coarse-grained sediments) in the slide could then be tracked by electrical resistivity measurements.

During the last 20 years, ERT has been increasingly applied to image the structure of landslides within soils and/or fine-grained formations (e.g. Jongmans and Garambois 2007; Loke et al. 2013; Perrone et al. 2014). The fundamentals of ERT prospecting are described in numerous books (e.g. Reynolds 1997) and will not be presented here. Thirty-one ERT profiles (see location in Fig. 2) were conducted over the landslide in order to get a global view about the resistivity variations in the first tens of metres below the ground surface. The Wenner or the Wenner-Schlumberger arrays were used with an electrode spacing of 1.5 to 5 m. Depending on the number of electrodes (ranging from 32 to 80), the profiles extend between 95 and 395 m in length (and up to 710 m for one where roll-along was possible to conduct). The high water content and clayey nature of the ground allowed a very good electrical coupling between the electrodes and the ground (electrode contact resistance between 200 and 400 Ω), generating a high signal to noise ratio for measurements. The electrical profiles were located using a GPS and the topographic profiles were extracted from a LiDar DTM available for the site (Bièvre et al. 2011). Apparent resistivity data were then inverted with the algorithm developed by Loke and Barker (1996). The L1 norm was used to sharpen the transition between adjacent lithological units. Acceptable absolute errors (lower than 5 %) between experimental and calculated apparent resistivities were reached after a maximum of three iterations.

Hydrogeological tests

Hydrogeological infiltration tests were carried at five sites exhibiting different slide velocity values and geophysical properties. The objective was to relate variations in slide velocities and geophysical properties to hydrogeological characteristics. The technique used, known as the Beerkan infiltration method, was pioneered by Braud et al. (2005) and has been successively improved by Lassabatère et al. (2006) and Yilmaz et al. (2010). It consists of measuring the time required for the 3D infiltration of successive known volumes of water (in this work, 100 to 200 ml, depending on the grain size) through a single annular ring (15 cm in diameter). The cylinder is inserted into the soil at a depth of around 1 cm to prevent lateral loss. A first volume of water is poured into the ring and the time needed for the complete infiltration is measured. Once the first volume of water is entirely infiltrated, a second volume of water is poured into the ring and the time for the complete infiltration is measured. In this experiment, 5 to 15 successive infiltrations were made, depending on the soil hydraulic conductivity. The soil is sampled in the immediate vicinity of the test to determine the initial natural gravimetric water content (w_s). A known volume of soil is also taken below the ring at the end of the experiment to determine the particle size distribution, the dry bulk density (ρ_s) and the saturated volumetric water content (θ_s). In this work, infiltration experiments were conducted after digging out 20 to 30 cm in order to avoid the root zone. For short times, the water infiltrates through the unsaturated soil in transient regime, whereas the infiltration at longer times occurs in a saturated soil in steady-state regime. The cumulative water height is plotted as a function of time, and the steady-state infiltration rate (SIR) is derived measuring the slope of the experimental infiltration curve at a steady-state regime. Experimental data (SIR, w_s, ρ_s, θ_s and the particle size distribution) are then used to compute the saturated hydraulic conductivity (K_s) applying the BEST algorithm (Lassabatère et al. 2006).

Results

Slide velocity

The surface velocity map, giving the mean annual horizontal velocity values interpolated from the 38 geodetic stations, is shown in Fig. 3a, along with the horizontal velocity vectors. The figure indicates a predominant eastward motion, associated to an increase in velocity, from 0–1 cm/year at the top of the landslide to more than 10 cm/year in its lower part. A southward increase in velocity is also visible in the lower part of the landslide where an active zone with velocity higher than 10 cm/year was recently detected (Bièvre et al. 2012). The topography along the two profiles AB and CD (see location in Fig. 3a) is plotted in Fig. 3b. The two profiles exhibit a similar topography with a mean slope of 11° below the Sinard plateau located at about 810 m asl and the presence of internal scarps. It is noticeable that no major change in slope angle is observed along the morainic and clayey parts of the sections (Fig. 3b).

The surface roughness map of the landslide (Fig. 3c; Kniess et al. 2014) shows that the roughness is generally low (RMSD <0.2 m) in the upper (western) part of the landslide, except along some hectometre-size scarps, and is higher (from 0.25 to 0.6 m) in the lower part of the landslide and in the gullies carved in the compact alluvium around the lake. Comparison of roughness and slide velocity maps (Fig. 3a, b, respectively) indicate that, at the first order, the higher the velocity, the higher the roughness is. Roughness values versus elevation are plotted along the two profiles AB and CD in Fig. 3d. After smoothing, both roughness curves show a break at about 700 m asl, with a sharp increase in roughness downslope. Slide velocity values are plotted against elevation for the 38 geodetic stations in Fig. 3e. Data points exhibit the same trend as in Fig. 3d, with a break at about 700 m asl and an increase in slide velocity below this value. Finally, an outlier with a high slide velocity value is visible at around 685 m asl (station g2 in Fig. 3a). Its origin will be assessed further.

Observation of the slide velocity and roughness in map views (Fig. 3a, c) and along two profiles (Fig. 3d, e) has pointed to a trend between the two parameters, with a threshold elevation value (700 m asl) separating upper weakly deformed zones from the more active and rougher ones in the lower part of the landslide. In the southern part of the landslide, the roughness is globally higher except for the presence of a small isolated zone of low roughness (red rectangle, Fig. 3a, c). This issue will be discussed later in the paper ("Discussion" section).
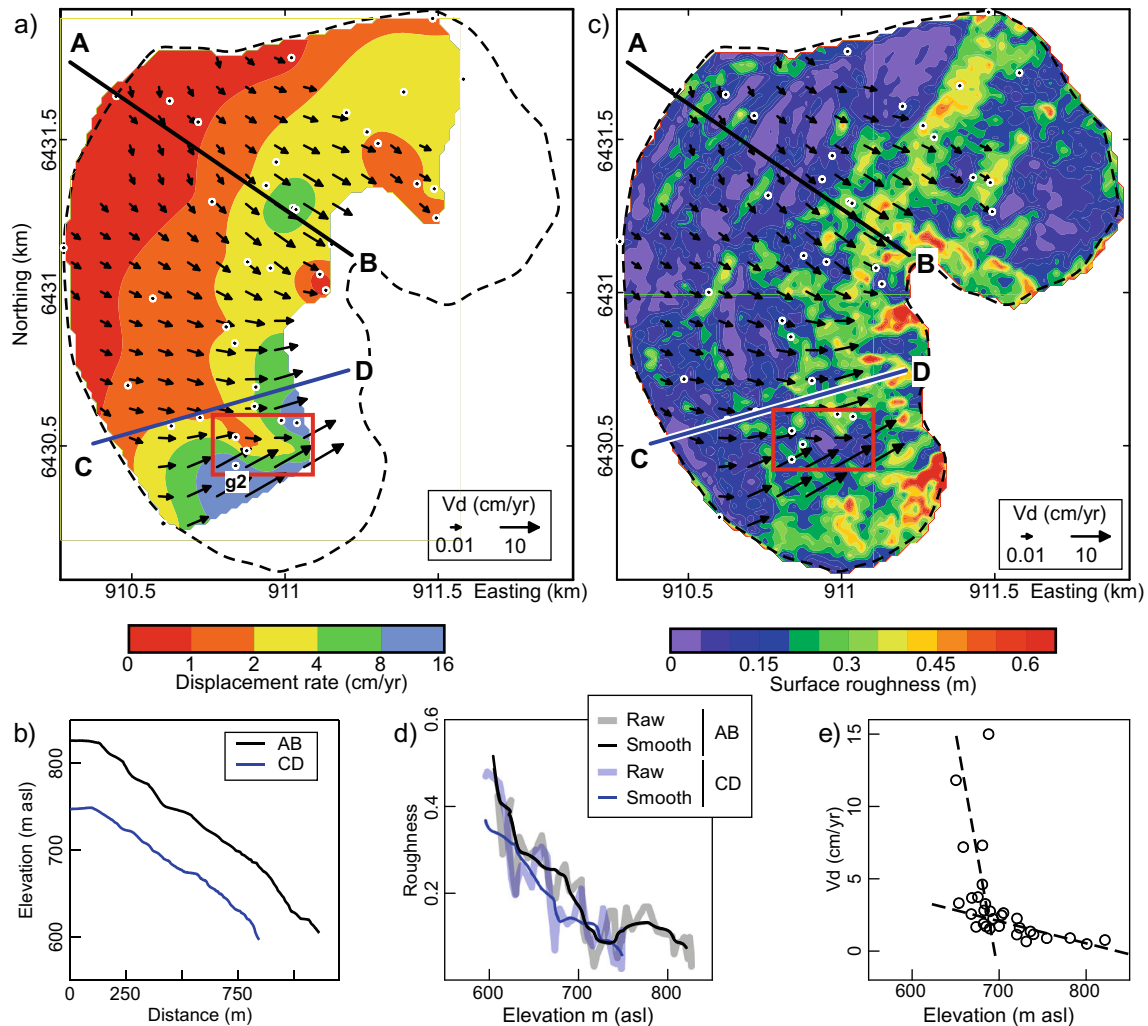
Fig. 3 Kinematics and morphological analysis. **a** Interpolated map of the horizontal mean annual velocity values derived from the 38 geodetic stations (*dots*). *Red rectangle*: see text for details. **b** Topographic profiles AB and CD (location in **a**). *Red rectangle*: see text for details. **c** Surface roughness map obtained from a LiDAR DTM acquired in 2006 (Kniess et al. 2014). **d** Evolution of roughness as a function of elevation along profiles AB and CD (location in **c**). **e** Mean annual horizontal velocities at the 38 geodetic stations as a function of elevation. *Black dashed lines* represent the linear trends below and above elevation of about 700 m asl

Electrical resistivity tomography results

Eleven electrical images (labelled E1 to E11, see location in Fig. 2) have been selected out of the 31 profiles acquired. The choice was made to illustrate the spatial resistivity variations over the land-slide. The characteristics of the ERT profiles are given in Table 1. As measurements were carried out at varying periods of the year, the shallow vadose zone is affected by hydrometeorological conditions (water content and temperature), agricultural works and cracks induced by the landslide. As these phenomena are likely to influence resistivity measurements, this zone of a maximum thickness of a few metres is not considered in this study.

The 11 selected electrical images are presented in Fig. 4 with a common resistivity scale. Resistivity values range from 5 to 700 Ω m; they exhibit a contrast between the southern and northern parts of the slide on the one hand and between the uphill and downhill parts on the other. To the north (profiles E1 to E5; Fig. 4a, b, c, d, e), the resistivity for an elevation higher than about 700 m ranges from 75 up to 100 Ω m. Of particular interest is the profile E5 which shows the continuity of the resistive layer up to

the Sinard plateau at an elevation of 800 m asl. The limited penetration (40 m), however, prevents from detecting the layer base in the western part of the profile.

Below 700 m asl, resistivity decreases rapidly to 35–70 Ω m, indicating the presence of finer grained material. To the south, this shallow resistive layer progressively vanishes, along with a slight deepening of its base from 700 to 680 m (E6 and E7; Fig. 4f, g), and the ground evolves to a totally conductive formation (E8, E9 and E10; Fig. 4h, i, j) with resistivity values mostly ranging from 20 to 40 Ω m. These low values correspond to the saturated laminated clays (LC), as evidenced by previous geophysical and geological studies in this area (Jongmans et al. 2009; Bièvre et al. 2012). The local resistivity variations (up to 60 Ω m) observed in the laminated clay layer probably result from the presence of a varying percentage of rock blocks and gravel in this formation, as found in borehole B4 (Bièvre et al. 2012). Along profile E11 (Fig. 4k), resistivity values dramatically increase to 700 Ω m below 530–540 m asl, in the weathered part of the top of the Mesozoic bedrock (MB) that outcrops nearby (Fig. 1a).

Table 1 Characteristics of electrical resistivity tomography profiles E1 to 11

Profile	Number of electrodes	Electrode spacing (m)	Profile length (m)	Number of Measurements	Number of Iterations	Absolute error (%)
E1	64	5	315	651	3	2.2
E2	64	5	315	647	3	2.4
E3	48	5	235	358	3	3
E4	48	5	235	359	3	1.4
E5*	144	5	710	2660	3	4.8
E6	48	5	235	360	3	2.4
E7	32	4	124	153	3	2.1
E8	64	3	189	1392	3	3
E9	80	5	395	884	3	1.98
E10	48	5	235	315	2	1.7
E11	64	5	315	540	3	4.9

Profile E5 was acquired in a roll-along mode

To avoid the effect of seasonal and anthropogenic variations at the surface, resistivity values at 10-m depth were extracted from the 31 ERT profiles. The 2550 points were then krigged using an experimental variogram and a mesh size of 20×20 m. The root mean square error (RMSE) between experimental and krigged values is 5.8 %. The resulting contour map (Fig. 5a) shows the presence of resistivity gradients with a decrease from north to south as well as from west to east. In both directions, the ground resistivity, which is over 75 Ω m above 700 m asl, gradually decreases to less than 40 Ω m below this elevation. These observations are detailed in the three cross sections AB, CD and AE (Fig. 5b). Profiles AB and AE highlight the strong resistivity decrease eastwards and southwards. The profile CD is located in the southern conductive area and exhibits resistivity values twice as low as the ones along the two other profiles.

In summary, ERT results show significant N-S and E-W downhill resistivity decreases within the Avignonet landslide. A resistive (>75 Ω m) layer covering one third of the landslide surface is detected above 700 m asl in its north-western more elevated part. The elevation of this boundary gently decreases southwards to 680 m. Its thickness varies between 0 and 40 m over the site and pinches downslope, laterally passing to laminated clays (resistivity ranging between 15 and 50 Ω m). To the east, this transition is marked by the presence of three non-perennial springs (labelled S in Fig. 1a) located at elevations of 715, 710 and 705 m asl from north to south, respectively. It is noticeable that spring elevations decrease from north to south along with the slight deepening of the base of the resistive layer. These observations suggest that the measured differences in resistivity might also be related to a hydrogeological interface located at these elevations, with an upper permeable layer overlying the impervious laminated clays. The detection of this thick upper resistive layer in the north-western part of the slide, which is not mapped on the geological map (see white dashed line in Fig. 1a), was unexpected and its origin will be discussed in the "Discussion" section.

Hydrogeological tests

Five superficial hydrogeological infiltration tests (i1 to i5) were carried out in different zones of the landslide exhibiting varying slide velocities and geophysical properties (see location in Fig. 5a) in order to measure the hydrogeological properties of the different identified layers. These tests were conducted at a few tens of centimetre depth, as no boreholes were available.

Test i1 was positioned at an elevation of 720 m asl along profile E4 (Fig. 4c), where the resistive layer outcrops. This elevation also corresponds to the altitude of two water catchments and of a spring (S in Fig. 5). Test i2 is located further down the slope along the same profile, in the clay layer. Test i3 was performed further to the south, close to GPS station AVN and at the limit of the resistive layer. The last two tests (i4 and i5) were conducted in the south of the Avignonet landslide, at the vicinity of the active zone where low resistivity levels are found ($\rho < 30$ Ω m; Fig. 5).

Laboratory geotechnical tests were performed on soil samples at the infiltration sites and results are given in Table 2. Cumulative infiltration curves as a function of time are shown in Fig. 6 and the computed hydraulic properties are provided in Table 2. For test i1, a fast infiltration rate ($SIR=1\times10^{-4}$ m/s) and a high hydraulic conductivity ($K_s=2.1\times10^{-5}$ m/s) were measured, consistently with the high porosity and the grain size distribution (more than 50 % of the soil is made of sand and gravel; Table 2). In contrast, infiltration test i2, carried out further downhill in the electrically conductive zone, yields a very low K_s value (8.1×10^{-7} m/s) in a soil mainly composed of clay and silts (65 %). Southwards (test i3), a finer material was also found (almost 66 % of clays and silts), yielding a low K_s value (2×10^{-6} m/s). These results are in agreement with the southward and downslope pinching out of the resistive and coarser grained layer. For tests i4 and i5, infiltration curves (Fig. 5) are curved, suggesting a double permeability (at the scales of both the matrix and the fissures) which prevents determination of the hydraulic conductivity. SIR values of 4×10^{-5} and 4×10^{-6} m/s (4×10^{-5} and 1×10^{-5} m/s) were computed at i4 (i5) for short and long times, respectively (Fig. 6). These values are relatively high, particularly at site i5, where nearly 92 % of the soil is made of silts and clays (Table 2). This apparent discrepancy
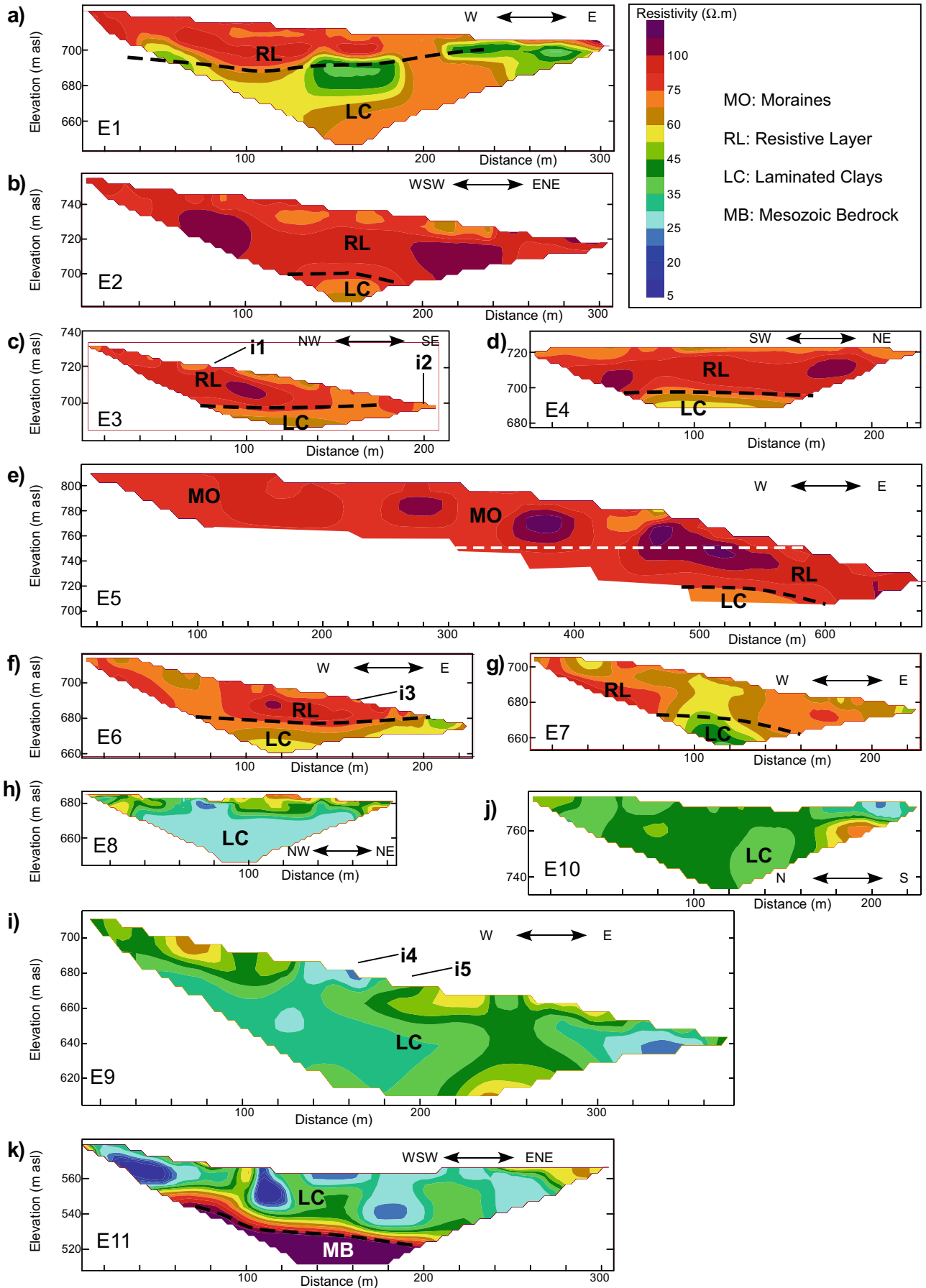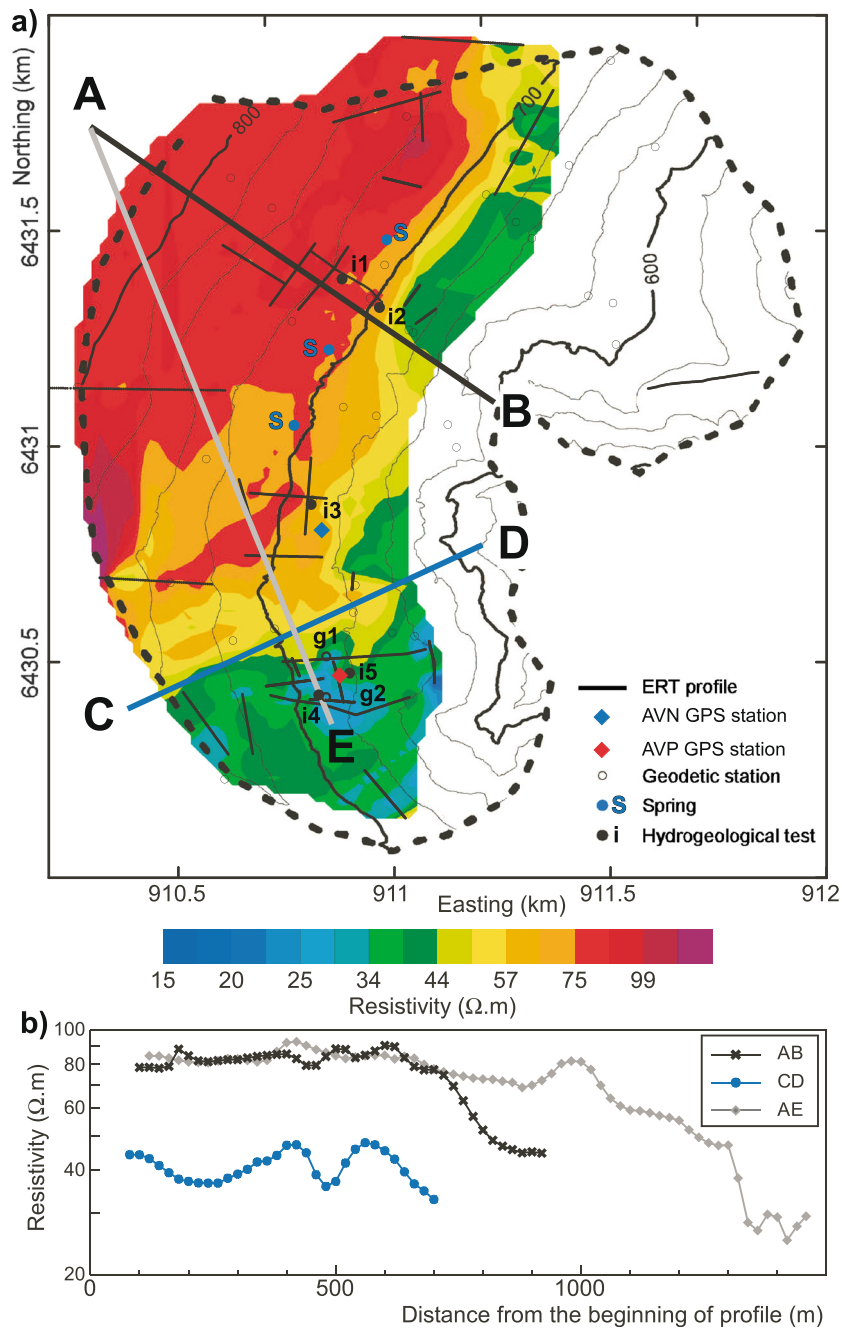
Fig. 5 Resistivity at 10-m depth over the Avignonet landslide. **a** Resistivity map is underlain by topographic contour lines in *black* (one contour line each 25 m). The location of the ERT profiles at 10-m depth is indicated (see Fig. 2 for their name). **b** Resistivity cross sections AB, CD and AE (location in Fig. 1a)

probably results from the presence of numerous superficial fissures in this active zone (Bièvre et al. 2012), which have increased the infiltration rates. Short-term higher values of *SIR* then probably correspond to the fissure permeability, while the long-term lower ones reflect water infiltration through both the fissures and the soil matrix.

◄ **Fig. 4** Electrical resistivity tomography profiles (location in Fig. 2). Absolute errors are lower than 5 % after a maximum of three iterations (details are provided in Table 1). Location of hydrogeological tests i1 to i5 is indicated. **a** Profile E1. **b** Profile E2. **c** Profile E3. **d** Profile E4. **e** Profile E5. The *white dashed line* represents the top of LC after Monjuvent (1973). **f** Profile E6. **g** Profile E7. **h** Profile E8. **i** Profile E9. **j** Profile E10. **k** Profile E11. *MB* Mesozoic bedrock, *LC* laminated clays, *RL* resistive layer, *MO* moraines

SIR values for tests i4 and i5 are in agreement with previous work (Bièvre et al. 2012) which yielded equivalent values (3×10^{-5} to 7×10^{-5} m/s) with permanent hydrogeological monitoring probes installed in the vicinity of the two infiltration tests. On the contrary, in situ Lefranc permeability tests conducted in drillings by Vuillermet et al. (1994) provided lower K_s values (3.6×10^{-9} to 4.1×10^{-9} m/s). This discrepancy could be partly explained by the more confined conditions of these tests compared to superficial ones. Above all, these tests were performed 10 km south of Avignonet in a more distal location where the soil is finer and made of 90 % of clays and 10 % of silts (Vuillermet et al. 1994; Brocard et al. 2003).

Table 2 Geotechnical and hydrogeological properties measured at the five infiltration sites.

Test	Granulometry (%)			Bulk density (g/cm³)	Dry bulk density (g/cm³)	Volumetric water content (%)	Porosity (%)	Permeability type	SIR (m/s)	K_s (m/s)
	Silt/Clay	Sand	Gravel							
I1	47.3	27.3	25.4	1.49	1.09	18.24	58.9	Matrix	1×10^{-4}	2.1×10^{-5}
I2	64.5	20.3	15.2	1.84	1.57	27.50	40.8	Matrix	3×10^{-6}	8.1×10^{-7}
I3	66.5	18.4	15.1	1.67	1.44	23.23	45.7	Matrix	1×10^{-5}	2×10^{-6}
I4	65.8	20.6	13.6	1.44	0.92	16.47	65.3 / FM	Fissures / 4x10-6	4×10^{-5} / X	X
I5	91.2	4.6	4.6	2.09	1.39	31.67	47.5	Fissures / FM	4×10^{-5} / 1×10^{-5}	X / X

Grain size distribution is expressed as weight percentage of soil type, according to the Wentworth scale (Wentworth 1922). Steady-state infiltration rates (SIR) are derived from Beerkan infiltration experiments (Fig. 6) and saturated hydraulic conductivities (K_s) are obtained by BEST inverse analysis

FM fissure and soil matrix, *X* BEST inverse analysis not possible (double permeability)
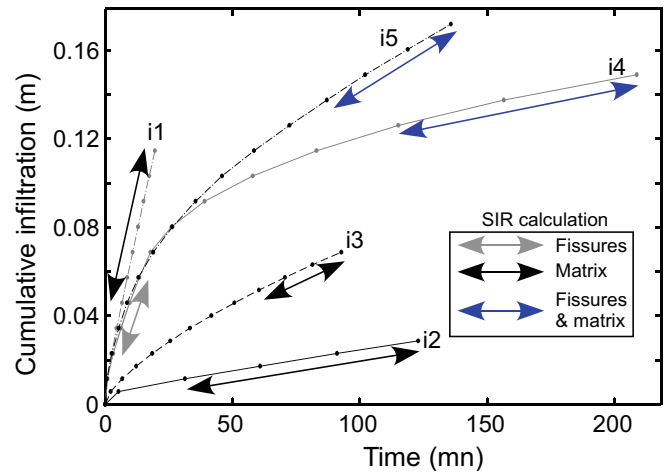
Fig. 6 Hydrogeological tests. Infiltration curves for tests i1 to i5 (see location in Fig. 5a). Steady state infiltration rates (SIR given in Table 2) were deduced from the curve parts shown with *double-arrowed lines*

The infiltration tests, even if they are limited in number, point to the heterogeneous hydrogeological properties of the superficial layers affected by the Avignonet landslide. First, the results show a contrast in K_s of at least one order of magnitude between the upper resistive ($\rho > 75$ Ω m; $K_s = 2.1\times10^{-5}$ m/s) coarser layer and the lower conductive ($\rho < 50$ Ω m; 0.8 to 2×10^{-6} m/s) clayey formation. These low values are interpreted as characterizing the matrix permeability. In the more deformed southern zone, infiltration tests (i4 and i5) revealed a distinct hydrogeological behaviour with a double permeability within a highly fissured matrix.

Discussion

The morphological and kinematical analysis has revealed a boundary defined by a change in slide velocity and surface roughness at an elevation around 700 m asl. Above this elevation, slide velocity is moderate (<5 cm/year) and surface roughness is low. Below this elevation, slide velocity increases rapidly to more than 10 cm/year and surface roughness is high, indicating a strongly deformed ground surface. The electrical survey has detected the unsuspected presence of a superficial resistive layer (75 to 100 Ω m) in the north-western part of the landslide. This layer overlies the electrically conductive laminated clays (15–50 Ω m) at an elevation decreasing from north (700 m asl) to south (680 m asl). In agreement with resistivity values, soil identification tests and superficial hydrogeological tests indicate that the layer is made of coarser material (i.e. sandy to gravelly clay) with permeability much higher than in the underlying clays. This lithological contact and the resulting vertical contrast in permeability are consistent with the alignment of several springs and catchments at elevations deepening from north (715 m asl) to south (705 m asl; Fig. 1a). This resistive layer can then be considered as an aquifer, the base of which is located at the top of the impermeable laminated clays.

At this time, the origin of this resistive layer remains uncertain. From the geological map (Fig. 1a; Debelmas 1967) and from several cross sections in the area (Monjuvent 1973), the Sinard plateau is covered by moraine deposits at an elevation of about 750 m asl. The first hypothesis is that the resistive formation is made of creeping moraine material mixed up with laminated clays on the slope. The second hypothesis is that this coarser layer could come from a former gravitational movement having affect-

ed the Sinard plateau. However, ERT profiles E1 to E7 (Fig. 4) evidenced a regular and sub-horizontal contact with respect to their resolution. Furthermore, ERT profile E5 (Fig. 4e) does not detect a horizontal interface at 750 m asl (white dashed line in Fig. 4e). On the contrary, it shows a lateral continuity between the identified resistive layer and the upper moraines covering the Sinard plateau. The simplest interpretation is that this resistive layer is the bottom of the moraines, which could then reach a thickness of up to 120 m. Further investigation including drilling should be conducted to assess the origin of this resistive layer.

The determined K_s value ($2{\times}10^{-5}$ m/s; test i1 in Fig. 6) as well as the great moraine thickness (up to 120 m) makes of this layer a considerable aquifer permanently supplying water that might infiltrate into the unstable underlying laminated clays. Water predominantly runs off the impervious surface or flows in the thin colluvium layer and infiltrates downslope in the vertical fissures induced by the gravitational movement. The presence of such fissures is attested by morphological observations and by previous geophysical and geotechnical studies. In the southern highly deformed zone of the slide, Bièvre et al. (2012) identified numerous open fissures of several metres long, which reach the water table at a depth of at least 2.5 m. This hydrogeological conceptual mechanism, already evidenced in previous pieces of work (van Genuchten and van Asch 1988; Vuillermet et al. 1994; van Asch et al. 1996; Bièvre et al. 2012; van der Spek et al. 2013), contributes to the slope destabilization which, in turn, favours vertical water infiltration. The key point here is that the upper part of the landslide is made of moraines and that this geological structure allows explaining the patterns in electrical resistivity, roughness and slide velocity over the landslide. Further evidence came from the more southerly part of the landslide where moraines are interpreted as being nearly absent (see the white dashed line in Fig. 1a) because of low electrical resistivity suggesting the presence of laminated clays; Fig 1a) and where slide velocity is slightly higher than in the northern upper part of the slide (Fig. 2a).

Considering the ground electrical conditions of the resistivity measurements at the Avignonet landslide, resistivity variations can be related to porosity and to the amount of clay (Archie 1942; Mavko et al. 2009). An increase in clay content and/or porosity results in a decrease in resistivity and vice versa. Such relationships between electrical and hydrogeological properties have already been reported in several in situ experiments in fine-grained landslides (Friedel et al. 2006; Di Maio and Piegari 2011; Lee et al. 2012). Moreover, these relationships have also been demonstrated experimentally in controlled laboratory experiments (among others: Abu-Hassanein et al. 1996a, b; Slater and Lesmes 2002; Tabbagh and Cosenza 2007). More particularly, Abu-Hassanein et al. (1996a) showed that resistivity decreases as the percentage of clay increases and as the associated hydraulic conductivity decreases. Resistivity might then be used as a proxy for lithological (and hydrogeological) variations at the scale of the Avignonet landslide. Figure 7 presents the horizontal slide velocity measured at the geodetic stations as a function of gridded resistivity with a log-log scale. Horizontal error bars correspond to the 5.8 % RMSE associated with the resistivity gridding process (Fig. 5), while vertical error bars show the standard deviations of mean annual horizontal velocities, reflecting the seasonal and pluriannual velocity variations. Figure 7 shows that slide velocities regularly decrease as resistivity increases. The fitting of an exponential relationship (of the form $Vd=Ae^{B\rho}$; black dashed line in Fig. 7)
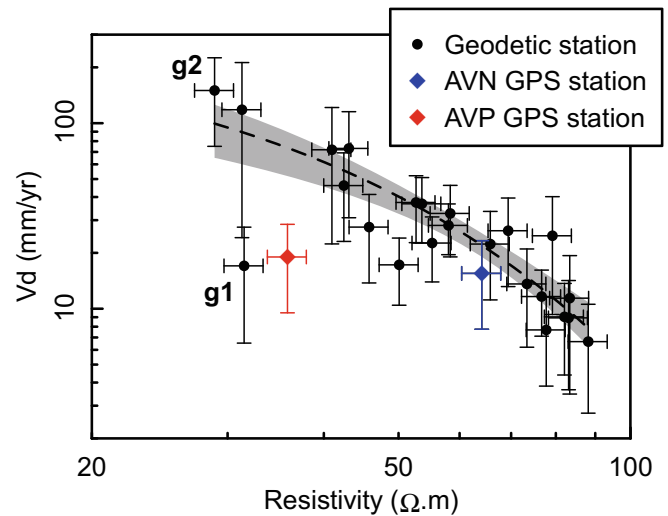

Fig. 7 Slide velocities as a function of resistivity at 10-m depth over the Avignonet landslide. The *black dashed line and the grey stripe* corresponds to the exponential law fit ($Vd=342e^{-0.043r}$) and to the 95 % confidence interval, respectively. The location of stations g1, g2, AVP and AVN is given in Fig. 5a

gave the parameters A=342 and B=−0.043. The coefficient of determination is 0.82. Although slide velocities are also controlled by other factors such as the geometry of the slip surface and of the topography, the forces acting on the slide (among others the effect of pore pressure) and the geotechnical parameters (cohesion and friction angle; Van Asch et al. 2006), they appear here to be partially related to resistivity distribution and consequently to grain size and hydraulic conductivity distribution.

However, two outliers, for which low velocity (<2 cm/year) and low resistivity (<40 Ω m) values are associated, are visible (Fig. 7) at the AVP GPS station and at the geodetic station g1, just to the north of AVP (location in Fig. 2). Considering their elevation below 700 m asl, these two stations are located within the laminated clays and should exhibit higher slide velocities. However, the surface roughness in this zone was found abnormally low ("Slide velocity" section, red rectangle in Fig. 3c). The picture of the site (Fig. 8) indeed shows a weakly deformed zone (including the stations g1 and AVP) in close proximity to strongly deformed areas characterized by higher slide velocities but similar low resistivity values (compare stations g1, g2 and AVP in Fig. 7). The apparent weak deformation of this zone remains unexplained but might be linked to the presence of nearly 30 m thick of reworked clays observed in
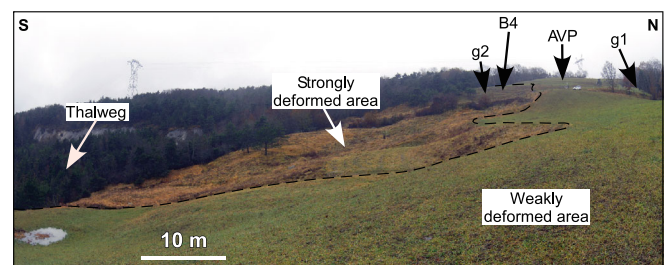

Fig. 8 Photograph taken from the toe of the Avignonet landslide (location is indicated as a *black star* in Fig. 2) and facing west. The 10-m-long *white bar* serves as a scale for the foreground

drilling B4 (Fig. 8; Bièvre et al. 2012). The disappearance of bedding and the presence of blocks might sign the presence of a former local gravitational movement which base would be located at an elevation of 665 m asl.

Conclusion

The combined interpretation of morphological, geodetic, electrical prospecting and hydrogeological data has brought a new insight in the hydromechanical mechanism of the large clayey Avignonet landslide, which was thought to develop mainly in lacustrine laminated clays. The performing of 31 electrical profiles all across the landslide has detected the presence of a thick resistive layer in its north-western more elevated part, covering one third of the landslide surface and overlying laminated clays at an elevation of about 700 m asl. This resistive layer is interpreted as the lower part of the moraines capping the Sinard plateau, which could then be 50 m thicker than previously thought. These coarser sediments are more hydraulically conductive than the laminated clays and constitute an aquifer, as attested by the presence of several springs aligned along the lithological contact. The major output of this study is to show that this lithological contact explains the main morphological features of the slope and control the kinematics of the landslide. Both roughness and slide velocity values show a dramatic change at the elevation of the lithological boundary, with an increase of these two parameters downslope. The interpretation is that the water in the upper aquifer discharges in the fissures initiated in the impervious clay layer, increasing pore water pressure and developing instability processes at different scales. The resulting slope deformation is consistent with the observed increase in roughness below 700 m asl. The coarser grain size distribution and the greater hydraulic conductivity in the moraines at the top of the slide prevent from high pore water pressure and induce surface deformation weaker than in the laminated clays outcropping downslope. The hydromechanical coupling, along with the landslide kinematics, then appears to be directly controlled by the Quaternary geological structure. This case study also illustrates how the initial understanding of a large landslide mechanism might be biased by the concentration of investigation in populated areas, here located in the southern clayey part of the slide. The study highlights the control of lithological variations on the landslide kinematics and the interest of using electrical resistivity tomography to map these variations in Quaternary sediments.

Acknowledgments

References

Abu-Hassanein Z, Benson C, Blotz L (1996a) Electrical resistivity of compacted clays. J Geotech Eng 122:397–406. doi:10.1061/(ASCE)0733-9410(1996)122:5(397)

Abu-Hassanein Z, Benson C, Wang X, Blotz L (1996b) Determining bentonite content in soil-bentonite mixtures using electrical conductivity. Geotech Test J 19:51–57

Aleotti P (2004) A warning system for rainfall-induced shallow failures. Eng Geol 73:247–265

Archie G (1942) The electrical resistivity log as an aid in determining some reservoir characteristics. Trans AIME 146:54–62

Baldi P, Cenni N, Fabris M, Zanutta A (2008) Kinematics of a landslide derived from archival photogrammetry and GPS data. Geomorphology 102:435–444. doi:10.1016/j.geomorph.2008.04.027

Bièvre G, Kniess U, Jongmans D, Pathier E, Schwartz S, van Westen C, Villemin T, Zumbo V (2011) Paleotopographic control of landslides in lacustrine deposits (Trièves plateau, French western Alps). Geomorphology 125:214–224. doi:10.1016/j.geomorph.2010.09.018

Bièvre G, Jongmans D, Winiarski T, Zumbo V (2012) Application of geophysical measurements for assessing the role of fissures in water infiltration within a clay landslide (Trièves area, French Alps). Hydrol Process 26:2128–2142. doi:10.1002/hyp.7986

Bovis M, Jones P (1992) Holocene history of earthflow mass movements in south-central British Columbia – the influence of hydroclimatic changes. Can J Earth Sci 29:1746–1755

Braud I, De Condappa D, Soria J, Haverkamp R, Angulo-Jaramillo R, Galle S, Vauclin M (2005) Use of scaled forms of the infiltration equation for the estimation of unsaturated soil hydraulic properties (the Beerkan method). Eur J Soil Sci 56:361–374. doi:10.1111/j.1365-2389.2004.00660.x

Brocard G, Van Der Beek P, Bourlès D, Siame L, Mugnier J (2003) Long-term fluvial incision rates and postglacial river relaxation time in the French Western Alps from 10Be dating of alluvial terraces with assessment of inheritance, soil development and wind ablation effects. Earth Planet Sci Lett 209:197–214

Chambers J et al (2011) Three-dimensional geophysical anatomy of an active landslide in Lias Group mudrocks, Cleveland basin, UK. Geomorphology 125:472–484. doi:10.1016/j.geomorph.2010.09.017

Coe J, McKenna J, Godt J, Baum R (2009) Basal-topographic control of stationary ponds on a continuously moving landslide. Earth Surf Process Landf 34:264–279. doi:10.1002/esp.1721

Corsini A, Pasuto A, Soldati M, Zannoni A (2005) Field monitoring of the Corvara landslide (Dolomites, Italy) and its relevance for hazard assessment. Geomorphology 66:149–165

Corsini A, Borgatti L, Coren F, Vellico M (2007) Use of multitemporal airborne LiDAR surveys to analyse postfailure behaviour of earthslides. Can J Remote Sens 33:116–120

Cruden D, Varnes D (1996) Landslide types and processes. In: Turner A, Schuster R (eds) Landslides investigation and mitigation. National Academic Press, Washington, pp 36–75

Daehne A, Corsini A (2013) Kinematics of active earthflows revealed by digital image correlation and DEM subtraction techniques applied to multi-temporal LiDAR data. Earth Surf Process Landf 38:640–654. doi:10.1002/esp.3351

Debelmas J (1967) La Chapelle-en-Vercors. In: Carte géologique de la France à 1/50000. BRGM Éditions, Orléans, France

Delacourt C, Allemand P, Bertier E, Raucoules D, Casson B, Grandjean P, Pambrun C, Varel E (2007) Remote-sensing techniques for analysing landslide kinematics: a review. Bull Soc Geol Fr 178:89–100. doi:10.2113/gssgfbull.178.2.89

Di Maio R, Piegari E (2011) Water storage mapping of pyroclastic covers through electrical resistivity measurements. Journal of Applied Geophysics 75:196–202. doi:10.1016/j.jappgeo.2011.07.009

Eilertsen R, Hansen L, Bargel T, Solberg I (2008) Clay slides in the Målselv valley, northern Norway: characteristics, occurrence, and triggering mechanisms. Geomorphology 93:548–562

Flageollet J, Maquaire O, Martin B, Weber D (1999) Landslides and climatic control conditions in the Barcelonnette and Vars basins (Southern French Alps, France. Geomorphology 30:65–78. doi:10.1016/S0169-555X(99)00045-8

François B, Tacher L, Bonnard C, Laloui L, Triguero V (2007) Numerical modelling of the hydrogeological and geomechanical behaviour of a large slope movement: the Triesenberg landslide (Liechtenstein). Can Geotech J 44:840–857. doi:10.1139/t07-028

Friedel S, Thielen A, Springman S (2006) Investigation of a slope endangered by rainfall-induced landslides using 3D resistivity tomography and geotechnical testing. Journal of Applied Geophysics 60:100–114. doi:10.1016/j.jappgeo.2006.01.001

Gerber R, Howard K (2000) Recharge through a regional till aquitard: three-dimensional flow model water balance approach. Ground Water 38:410–422. doi:10.1111/j.1745-6584.2000.tb00227.x

Giraud A, Antoine P, Van Asch T, Nieuwenhuis J (1991) Eng Geol 31:185–195. doi:10.1016/0013-7952(91)90005-6

Golden Software (2012) Surfer user manual. Golden Software, Golden

Guerriero L, Coe J, Revellino P, Grelle G, Pinto F, Guadagno F (2014) Influence of slip-surface geometry on earth-flow deformation, Montaguto earth flow, southern Italy. Geomorphology 219:285–305. doi:10.1016/j.geomorph.2014.04.039

Handwerger A, Roering J, Schmidt D (2013) Controls on the seasonal deformation of slow-moving landslides. Earth Planet Sci Lett 377–378:239–247. doi:10.1016/j.epsl.2013.06.047

Hungr O, Leroueil S, Picarelli L (2014) The Varnes classification of landslide types, an update. Landslides 11:167–194. doi:10.1007/s10346-013-0436-y

Iverson R (2000) Landslide triggering by rain infiltration. Water Resour Res 36:1897–1910

Iverson R (2004) Regulation of landslide motion by dilatancy and pore pressure feedback. J Geophys Res Earth Surf 110, F02015. doi:10.1029/2004JF000268

Iverson R, Major J (1987) Rainfall, groundwater-flow, and seasonal movement at Minor Creek landslide, northwestern California - Physical interpretation of empirical relations. Geol Soc Am Bull 99:579–594. doi:10.1130/0016-606(1987)99<579:RGFASM>2.0.CO;2

Jaboyedoff M, Oppikofer T, Abellán A, Derron M, Loye A, Metzger R, Pedrazzini A (2012) Use of LIDAR in landslide investigations: a review. Nat Hazards 61:5–28. doi:10.1007/s11069-010-9634-2

Jongmans D, Garambois S (2007) Geophysical investigation of landslides: a review. Bull Soc Geol Fr 178:101–112

Jongmans D, Bièvre G, Schwartz S, Renalier F, Beaurez N (2009) Geophysical investigation of the large Avignonet landslide in glaciolacustrine clays in the Trièves area (French Alps). Eng Geol 109:45–56. doi:10.1016/j.enggeo.2008.10.005

Keefer D (1984) Landslides caused by earthquakes. Geol Soc Am Bull 95:406–421

Keefer D (2002) Investigating landslides caused by earthquakes - a historical review. Surv Geophys 23:473–510

Kelsey H (1978) Earthflows in Franciscan melange, Van Duzen River basin, California. Geology 6:361–364. doi:10.1130/0091-7613(1978)6<361:EIFMVD>2.0.CO;2

Kniess U (2011) Quantification de l'évolution de glissements argileux par des techniques de télédétection. Application à la région du Trièves (Alpes Françaises occidentales). PhD thesis in English, Université de Grenoble, France.

Kniess U, Travelletti J, Daehne A, Krzeminska D, Bièvre G, Jongmans D, Corsini A, Bogaard T, Malet J (2014) Innovative techniques for the characterization of the morphology, geometry and hydrological features of slow-moving landslides. In: Van Asch T J W, Corominas J, Greiving S, Malet J-P, Sterlacchini S (eds.) Mountain risks: from prediction to management and governance. Springer Netherlands. pp. 57–82. doi:10.1007/978-94-007-6769-0_3

Lapenna V, Lorenzo P, Perrone A, Piscitelli S, Rizzo E, Sdao F (2005) 2D electrical resistivity imaging of some complex landslides in Lucanian Apennine chain, southern Italy. Geophysics 70:B11–B18

Lassabatère L, Angulo-Jaramillo R, Soria Ugalde J, Cuenca R, Braud I, Haverkamp R (2006) Beerkan estimation of soil transfer parameters through infiltration experiments - BEST. Soil Sci Soc Am J 70:521–532. doi:10.2136/sssaj2005.0026

Lebourg T, Hernandez M, Zerathe S, Bedoui S, Jomard H, Fresia B (2010) Landslides triggered factors analysed by time lapse electrical survey and multidimensional statistical approach. Eng Geol 114:238–250. doi:10.1016/j.enggeo.2010.05.001

Lee C, Zeng L, Hsieh C, Yu C, Hsieh S (2012) Determination of mechanisms and hydrogeological environments of Gangxianlane landslides using geoelectrical and geological data in central Taiwan. Environmental Earth Sciences 66:1641–1651. doi:10.1007/s12665-012-1522-5

Loke M, Barker R (1996) Rapid least-squares inversion of apparent resistivity pseudosections by a quasi-Newton method. Geophys Prospect 44:131–152

Loke M, Chambers J, Rucker D, Kuras O, Wilkinson P (2013) Recent developments in the direct-current geoelectrical imaging method. Journal of Applied Geophysics 95:135–156. doi:10.1016/j.jappgeo.2013.02.017

Lorier L, Desvarreux P (2004) Glissement du Mas d'Avignonet, commune d'Avignonet. In: Proceedings of the workshop Ryskhydrogeo, Program Interreg III, La Mure (France)

Mackey B, Roering J, McKean J (2009) Long-term kinematics and sediment flux of an active earthflow, Eel River, California. Geology 37:803–806. doi:10.1130/G30136A.1

Malet J, Maquaire O, Calais E (2002) The use of global positioning system techniques for the continuous monitoring of landslides: application to the Super-Sauze earthflow (Alpes-de-Haute-Provence, France). Geomorphology 43:33–54. doi:10.1016/S0169-555X(01)00098-8

Mavko G, Mukerji T, Dvorkin J (2009) The rock physics handbook, tools for seismic analysis of porous media, 2nd edition, Cambridge University Press, Cambridge

Monjuvent G (1973) La transfluence Durance-Isère. Essai de synthèse du Quaternaire du bassin du Drac (Alpes françaises). Géol Alpine 49:57–118

Moulin C, Robert Y (2004) Le glissement de l'Harmalière sur la commune de Sinard. In: Proceedings of the workshop Ryskhydrogeo, Program Interreg III, La Mure (France), 11 pp

Oppikofer T, Jaboyedoff M, Keusen H (2008) Collapse at the eastern Eiger flank in the Swiss Alps. Nat Geosci 1:531–535. doi:10.1038/ngeo258

Perrone A, Lapenna V, Piscitelli S (2014) Electrical resistivity tomography technique for landslide investigation: a review. Earth Sci Rev 135:65–82. doi:10.1016/j.earscirev.2014.04.002

Petley D, Mantovani F, Bulmer M, Zannoni A (2005) The use of surface monitoring data for the interpretation of landslide movement patterns. Geomorphology 66:133–147. doi:10.1016/j.geomorph.2004.09.011

Picarelli L (2000) Mechanisms and Rates of Slope Movements in Fine Grained Soils. In: Proceedings of the International Conference on Geotechnical and Geological Engineering, GEOENG2000, Melbourne, Australia. pp. 1618–1670

Picarelli L, Urciuoli G, Russo C (2004) The role of groundwater regime on behaviour of clayey slopes. Can Geotech J 41:467–484

Renalier F, Bièvre G, Jongmans D, Campillo M, Bard P (2010a) Characterization and monitoring of unstable clay slopes using active and passive shear wave velocity measurements. In: Miller R, Bradford J, Holliger K (eds) Advances in near-surface seismology and ground-penetrating radar. Society of Exploration Geophysics, Tulsa, pp 397–414. doi:10.1190/1.9781560802259.ch24

Renalier F, Jongmans D, Campillo M, Bard P (2010b) Shear wave velocity imaging of the Avignonet landslide (France) using ambient noise cross-correlation. J Geophys Res 115, F03032. doi:10.1029/2009JF001538

Reynolds J (1997) An introduction to applied and environmental geophysics. Wiley and Sons, Chichester

Rodriguez C, Bommer J, Chandler R (1999) Earthquake-induced landslides: 1980–1997. Soil Dyn Earthq Eng 18:325–346. doi:10.1016/S0267-7261(99)00012-3

Roering J, Stimely L, Mackey B, Schmidt D (2009) Using DInSAR, airborne LiDAR, and archival air photos to quantify landsliding and sediment transport. Geophys Res Lett 36, L19402. doi:10.1029/2009GL040374

Rott H, Scheuchl B, Siegel A, Grasemann B (1999) Monitoring very slow slope motion by means of SAR interferometry: a case study from a mass waste above a reservoir in the Otztal Alps, Austria. Geophys Res Lett 26:1629–1632. doi:10.1029/1999GL900262

Schwab M, Rieke-Zapp D, Schneider H, Liniger M, Schlunegger F (2008) Landsliding and sediment flux in the Central Swiss Alps: a photogrammetric study of the Schimbrig landslide, Entlebuch. Geomorphology 97:392–406. doi:10.1016/j.geomorph.2007.08.019

Shepard M, Campbell B, Bulmer M, Farr T, Gaddis L, Plaut J (2001) The roughness of natural terrain: a planetary and remote sensing perspective. J Geophys Res 106:32777–32795. doi:10.1029/2000JE001429

Slater L, Lesmes D (2002) Electrical-hydraulic relationships observed for unconsolidated sediments. Water Resour Res 38:31-1-31-13. doi: 10.1029/2001WR001075

Squarzoni C, Delacourt C, Allemand P (2003) Nine years of spatial and temporal evolution of the La Valette landslide observed by SAR interferometry. Eng Geol 68:53–66

Stiros S, Vichas C, Skourtis C (2004) Landslide monitoring based on geodetically derived distance changes. J Surv Eng 130:156–162

Strozzi T, Farina P, Corsini A, Ambrosi C, Thüring M, Zilger J, Wiesmann A, Wegmüller U, Werner C (2005) Survey and monitoring of landslide displacements by means of L-band satellite SAR interferometry. Landslides 2:193–201

Tabbagh A, Cosenza P (2007) Effect of microstructure on the electrical conductivity of clay-rich systems. Physics and Chemistry of the Earth, Parts A/B/C 32:154–160. doi:10.1016/j.pce.2006.02.045

Teza G, Pesci A, Genevois R, Galgaro A (2008) Characterization of landslide ground surface kinematics from terrestrial laser scanning and strain field computation. Geomorphology 97:424–437. doi:10.1016/j.geomorph.2007.09.003

Travelletti J, Sailhac P, Malet J, Grandjean G, Ponton J (2011) Hydrological response of weathered clay-shale slopes: water infiltration monitoring with time-lapse electrical resistivity tomography. Hydrol Process 26:2106–2119. doi:10.1002/hyp.7983

Travelletti J, Delacourt C, Allemand P, Malet J, Schmittbuhl J, Toussaint R, Bastard M (2012) Correlation of multi-temporal ground-based optical images for landslide monitoring: application, potential and limitations. ISPRS J Photogramm Remote Sens 70:39–55. doi:10.1016/j.isprsjprs.2012.03.007

Travelletti J, Malet J, Samyn K, Grandjean G, Jaboyedoff M (2013) Control of landslide retrogression by discontinuities: evidences by the integration of airborne- and ground-based geophysical information. Landslides 10:37–54. doi:10.1007/s10346-011-0310-8

Van Asch T, Hendriks M, Hessel R, Rappange F (1996) Hydrological triggering conditions of landslides in varved clays in the French Alps. Eng Geol 42:239–251

Van Asch T, Buma J, Van Beek L (1999) A view on some hydrological triggering systems in landslides. Geomorphology 30:25–32

Van Asch T, Malet J, Van Beek L (2006) Influence of landslide geometry and kinematic deformation to describe the liquefaction of landslides: some theoretical considerations. Eng Geol 88:59–69. doi:10.1016/j.enggeo.2006.08.002

Van Asch T, Van Beek L, Bogaard T (2007) Problems in predicting the mobility of slow-moving landslides. Eng Geol 91:46–55. doi:10.1016/j.enggeo.2006.12.012

Van Asch T, Malet J, Bogaard T (2009) The effect of groundwater fluctuations on the velocity pattern of slow-moving landslides. Nat Hazards Earth Syst Sci 9:739–749

Van der Spek J, Bogaard T, Bakker M (2013) Characterization of groundwater dynamics in landslides in varved clays. Hydrol Earth Syst Sci 10:295–324. doi:10.5194/hessd-10-295-2013

Van Genuchten P, Van Asch T (1988) Factors controlling the movement of a landslide in varved clays near La Mure (French Alps). Bull Soc Geol Fr 8:461–469

Varnes D (1978) Slope movement types and processes. In: Schuster R, Krizek R (eds) Landslides: analysis and control. National Academic Press, Washington, pp 11–33

Vuillermet E, Cordary D, Giraud A (1994) Caractéristiques hydrauliques des argiles litées du Trièves (Isère). Bull Int Assoc Eng Geol 49:85–90

Wang G (2011) GPS landslide monitoring: single base vs network solutions - a case study based on the Puerto Rico and Virgin Islands permanent GPS network. J Geod Sci 1:191–203. doi:10.2478/v10156-010-0022-3

Wentworth C (1922) A scale of grade and class terms for clastic sediments. J Geol 30:377–392

Yilmaz D, Lassabatère L, Angulo-Jaramillo R, Deneele D, Legret M (2010) Hydrodynamic characterization of basic oxygen furnace slag through an adapted BEST method. Vadose Zone J 9:107–116. doi:10.2136/vzj2009.0039

Zhang X, Phillips C, Pearce A (1991) Surface movement in an earthflow complex, Raukumara Peninsula, New Zealand. Geomorphology 4:261–272. doi:10.1016/0169-555X(91)90009-Y

G. Bièvre (✉) · D. Jongmans · E. Pathier
Université Grenoble Alpes, ISTerre,
38041, Grenoble, France
e-mail: gregory.bievre@ujf-grenoble.fr

D. Goutaland
Laboratoire de Clermont-Ferrand,
CEREMA,
63017, Clermont-Ferrand, France

V. Zumbo
SYSTRA,
75513, Paris, France